Oriented Crystallization of Mixed-Cation Tin Halides for Highly Efficient and Stable Lead-Free Perovskite Solar Cells

Oriented Crystallization of Mixed-Cation Tin Halides for Highly Efficient and Stable Lead-Free Perovskite Solar Cells

*Bin-Bin Yu, Min Liao, Yudong Zhu, Xusheng Zhang, Zheng Du, Zhixin Jin, Di Liu, Yiyu Wang, Teresa Gatti, Oleg Ageev, and Zhubing He**

Dr. B.-B. Yu, M. Liao, Y. Zhu, X. Zhang, Z. Du, Z. Jin, D. Liu, Y. Wang, Prof. Z. He
Department of Materials Science and Engineering
Shenzhen Key Laboratory of Full Spectral Solar Electricity Generation (FSSEG)

Southern University of Science and Technology 1088 Xueyuan Avenue, Shenzhen 518055, China E-mail: hezb@sustech.edu.cn
Dr. B.-B. Yu

Academy for Advanced Interdisciplinary Studies Southern University of Science and Technology 1088 Xueyuan Avenue, Shenzhen 518055, China Prof. T. Gatti

Center for Materials Research
Justus Liebig University
Heinrich Buff Ring 17, Giessen 35392, Germany Prof. O. Ageev
Institute of Nanotechnologies
Electronics and Equipment Engineering Southern Federal University
2 Shevchenko, Taganrog 347928, Russia

1. Introduction

Organic–inorganic lead halide perovskite solar cells (PSCs) have achieved up to 25.2% in conversion efficiency owing to their outstanding optoelectronic proper- ties and numerous efforts for the past 10 years.[1–9] However, the toxicity of lead is still deemed as a critical challenge for its future commercialization.[10,11] There- fore, low- or non-toxic perovskites have been extensively investigated to explore lead-free alternatives.[12–14] Among them, tin is viewed as the promising candidate to substitute lead in perovskites owing to their similar ionic structure,[10] achieving the highest conversion efficiency around 10% up to date.[15] However, tin halide perovskites suffer from the severe oxida- tion of Sn^{2+} to Sn^{4+}.[16] That leads to deep p-type self-doping, Sn vacancies, and possible Sn^{4+} impurity phase, which act as trap centers for the recombination of photogenerated charges,[17] and result in the unsatisfactory conversion efficiency far from what they deserve. In addition, that oxidation also accounts for the poor sta- bility of tin halide perovskites materials and devices. In order to suppress the Sn^{2+} oxidation of tin halide perovskites, increasing efforts have been made to improve the photovoltaic performance and stability of tin halide-based PSCs.[18–43] Some potential strategies to inhibit the oxidation of Sn^{2+} mainly include the introducing of reductant additives into perovskite precursor solutions,[18–21] composition engineering of alloying cations or anions,[23–27] adopting low-dimensional perovskites,[28,29] and etc. Because it owns the suitable bandgap (1.3–1.4 eV) and superior optoelectronic properties, formamidinium tin triiodide perovskite ($FASnI_3$) is deemed as one of the most promising candidates to enable high-performance tin halide based PSCs. Depending on those anti-oxidation strategies mentioned above, $FASnI_3$ based PSCs have achieved exciting progress.[24–39] Lee et al. found that the introduction of bromide anions into $FASnI_3$ can significantly decrease the Sn vacancies caused by Sn^{2+} oxidation and improved conversion efficiency to 5.5% with high stability.[25] Liu et al. achieved an impressive power conversion efficiency (PCE) of 9.06% based on FA MA SnI as a light absorber.[24] Recently, Ran et al. pushed its conversion efficiency up to 9.61% by introducing 3-phenyl-2-propen-1-amine with reduced trap density and pref- erential orientation of the perovskite.[35] It seems that either Br^- anion or MA^+ cation can improve the photovoltaic performance of tin halide perovskites by inhibiting Sn^{2+} oxidation.[22–25] However, the synergistic effect of both Br^- anion and MA^+ cation on the photovoltaic performance of $FASnI_3$ perovskites has never been reported to the best knowl- edge of us. They attract our eyesights because methylammo- nium bromide (MABr) is so general in the synthesis of lead halide perovskites. Actually, MABr alloyed lead perovskites ($(FAPbI_3)_{1-x}(MAPbBr_3)_x$) have been discovered to enhance phase stability and crystallinity,[3,44] to limit ionic drift and charge accumulation,[45] to improve film qualities by enlarged grain size and decreased pinholes[46] effectively. Those effects lead to dramatic enhancements of both efficiency and stability of MABr alloyed $FAPbI_3$-based PSCs. Hence, it is really impera- tive to explore the comprehensive effect of MABr on $FASnI_3$ perovskites.

In this work, we incorporated MABr into $FASnI_3$ pre- cursor solutions to fabricate both cation and anion mixed $MA_xFA_{1-x}SnI_{3-x}Br_x$ ($x = 0, 0.15, 0.25, 0.5, 1$) perovskites, excit- ingly obtaining a champion device conversion efficiency of 9.31% with negligible hysteresis, while that of the control device is 5.02%. Strikingly, the highly oriented growth of the tin halide perovskite films with high crystallinity was found to account for the remarkable augment in device performance

because that high film quality can decrease the defect density of the perov- skite films and hence reduce the recombination to large extent. Detailed structure characterizations were conducted to reveal the mechanism behind that impressive orientation as well as the bandgap modulation. Systematical optoelectronic charac- terizations discover the suppression of Sn^{2+}oxidation can also modulate the energy level structure of the alloyed perovskite and herein improve the band level alignment of the devices. Remarkably, the encapsulated $MA_{0.25}FA_{0.75}SnI_{2.75}Br_{0.25}$ device also exhibits high stability with maintaining above 80% of the initial conversion efficiency after 300 h light soaking.

2. Results and Discussion

Figure 1a shows the crystallinity evolution of $MA_xFA_{1-x}SnI_{3-x}Br_x$ perovskite films by alloying different composition of MABr with *x* ranging from 0 to 1. In the X-ray diffraction (XRD) patterns, all the diffraction peaks can be indexed to the orthorhombic $FASnI_3$, consistent with some previous reports.[18–20] Interest- ingly, with the increase of MABr in the composition, the peak intensities of (001) series are enhanced significantly, which demonstrates the high-orientation growth of the films. To dis- criminate the evolution course, the magnified XRD patterns of $MA_xFA_{1-x}SnI_{3-x}Br_x$ perovskite films with less *x* are shown in Figure 1b. We find the other peaks (111, 012, and 022) attenuate as *x* increases while the (001) series turn stronger and stronger. When FAI was completely replaced by MABr to form MAS- nI_2Br perovskite, only (001), (002), and (003) peaks are shown in the XRD pattern. No other peaks emerge, implying highly oriented growth of $MASnI_2Br$ perovskite film. In addition, apparent shifts to higher 2 degrees of all the peaks indicate the reduction of the lattice parameter after MABr incorpora- tion. That demonstrates clearly that MABr accounts for that high orientation growth and high crystallinity of those perov- skite films.[44] The high-resolution peak (001) at ≈14° further convinces the peak shift and Br alloying, shown in Figure S1, Supporting Information.

To clarify whether MA^+ or Br^- is directly responsible for this enhancement, FABr and MAI were incorporated into the com- pound as shown in Figure 1c. In contrast to MABr, the crystal- line orientation enhancement effect of FABr is poor, while MAI shows strong enhancing capability, as Figure 1c shows. Then, the corresponding concentration of MAI was incorporated into the compound, which leads to the impressive orientation enhancing effect (Figure 1d). That unambiguously proves that the MA^+ cation is responsible for the oriented crystallization of $MA_xFA_{1-x}SnI_{3-x}Br_x$ perovskite films.

The perovskite composition by incorporating MABr was further verified by time-of-flight secondary ion mass spectrom- etry (ToF-SIMS). Figure S2, Supporting Information shows the depth profiles of key elemental groups obtained from ToF-SIMS measurements of both the pristine $FASnI_3$ and the $MA_{0.25}FA_{0.75}SnI_{2.75}Br_{0.25}$ perovskite films deposited on ITO glass. The signals of MA^+ (CH_6N^+) and Br^- ions are clearly observed only in the $MA_{0.25}FA_{0.75}SnI_{2.75}Br_{0.25}$ film while the pristine $FASnI_3$ shows no signal of MA^+ or Br^-. In addition, it can also be observed that both MA^+ and Br^- are uniformly distributed throughout the $MA_{0.25}FA_{0.75}SnI_{2.75}Br_{0.25}$ perovskite film.

Figure 2a–e show the topographic morphology evolution of the $MA_xFA_{1-x}SnI_{3-x}Br_x$ perovskite films by incorporation of different composition of MABr successively. Those scanning electron microscopy (SEM) images show that all the films are compact, except for some pinholes observed in the $MASnI_2Br$ film (Figure 2e and Figure S3, Supporting Information). From Figure 2a,b, when MABr is added, the light flakes in the orig- inal $FASnI_3$ disappear. Meanwhile, the crystallinity of grains was improved obviously, which is in accordance to the improve- ment shown in the XRD patterns (Figure 1 and Table S1, Supporting Information). Further increasing the composition of MABr (Figure 2c), some part of grain size becomes larger and the crystallinity is also enhanced. When the MABr composi- tion arrives to 0.5 (Figure 2d), the larger grains turn to merge with each other, and it forms into the "molten" and flat film when FAI is substituted by MABr totally in the $MASnI_2Br$ film (Figure 2e). It is really interesting for tin halide perovskite films,[27] and here we attribute this oriented crystallization growth of $FASnI_3$ to the function of MA^+ cation. The detailed mechanism behind is still under exploring.

As we concern, the absorption spectra of the typical $MA_xFA_{1-x}SnI_{3-x}Br_x$ perovskite films with different composition ofMABrwererecordedbytheUV–visspectrometerandshown in Figure 2f. The absorption onset of $MA_xFA_{1-x}SnI_{3-x}Br_x$ films shifts from ≈922 nm (black line) to ≈798 nm (rose red line) when the *x* increasing from 0 to 1. Obviously, the alloying of both MA^+ and Br^- definitely accounts for blue shifts in the optical bandgaps, which is consistent with the former lit- eratures.[25,43] Deduced from the corresponding Tauc plots in Figure S4, Supporting Information, the bandgaps of $MA_xFA_{1-x}SnI_{3-x}Br_x$ perovskite films with $x = 0.15, 0.25, 0.5, 1$ are determined as 1.42, 1.44, 1.47, and 1.55 eV, compared with 1.34 eV of pristine $FASnI_3$ film. Meanwhile, owing to the improved crystallinity by the incorporation of MABr, the absorption coefficients at the edge are obviously enhanced as the inset picture shows (Figure 2f), which definitely benefits their based device performances.

In order to reveal the electronic structures of the pristine $FASnI_3$ and $MA_{0.25}FA_{0.75}SnI_{2.75}Br_{0.25}$ perovskite films, their ultraviolet photoelectron spectroscopy (UPS) spectra are shown in Figure S5, Supporting Information. The work functions ( ) of the pristine $FASnI_3$ and $MA_{0.25}FA_{0.75}SnI_{2.75}Br_{0.25}$ perovskite films can be determined as −4.94 and −4.53 eV, respectively. The corresponding valence band maximum values are deter- mined at −5.33 and −5.02 eV, respectively, resulted from the tail of the UPS spectra in Figure S5, Supporting Information. Then, according to the data obtained from Figure S4, Sup-

porting Information, the conduction band minimum (CBM) of them can be calculated as −3.99 and −3.58 eV, respec- tively. Finally, the energy band level structure of their based inverted planar devices can be constructed. In the device band alignment (**Figure 3**a), $MA_{0.25}FA_{0.75}SnI_{2.75}Br_{0.25}$ matches better with both the hole-transport layer (HTL, Poly(3,4-ethylenedioxythiophene)-poly(styrenesulfonate) (PEDOT:PSS)) and the electron-transport layer ([6,6]-Phenyl C_{61} butyric acid methyl ester (P_{61}CBM)) than $FASnI_3$, and herein owns stronger carrier transportability at the bi-interfaces, resulting ration- ally in the improved device performance. Figure 3b shows the cross-sectional SEM image of the typical device with a configu- ration "ITO/PEDOT:PSS/perovskite/PC_{61}BM/BCP/Al/Ag" as shown in Figure 3a, where the thickness of perovskite layer is about 260 nm while the PEDOT:PSS and PCBM layers have the thickness of around 50 nm. In addition, a combination film of BCP (≈8 nm) and Al/Ag (≈70 nm) was utilized as the rear elec- trode in device.

To investigate the effect of the incorporation of MABr to $FASnI_3$ perovskite, the current density–voltage (J–V) curves in forward scan of the $MA_xFA_{1-x}SnI_{3-x}Br_x$-based champion devices are tested under a standard simulated solar illumina- tion (AM 1.5 G, 100 mW cm^{-2}) (Figure 3c). The best device con- version efficiency of $MA_{0.25}FA_{0.75}SnI_{2.75}Br_{0.25}$-based PSCs with x = 0.25 arrives to 9.31%, with an open circuit (V_{oc}) of 0.60 V, a short circuit current density (J_{sc}) of 22.48 mA cm^{-2} and a fill factor (FF) of 0.69. In comparison, the control $FASnI_3$ based device got the best conversion efficiency of 5.02% along with the J_{sc} of 21.82 mA cm^{-2}, V_{oc} of 0.39 V, and FF of 0.59. Both V_{0C} and FF show significant enhancement while J_{sc} increases a little. As discussed above, the bandgap increases after alloying $FASnI_3$ with MABr (Figure 2f). Interestingly, when x increases from 0 to 0.25 in $MA_xFA_{1-x}SnI_{3-x}Br_x$ perovskites, it seems that J_{SC} should decrease because the bandgap augment would result in less absorption of photons. However, with the alloy of 0.25 MABr, the film quality of the mixed perovskite was improved much and definitely decreased defects density, which would increase the J_{SC} by suppressing irradiative recombina- tion. It is obvious that the improved film crystallinity discussed above reduces the trap density by function of MABr, which defi- nitely enlarges FF and V_{oc} too. Besides of that, the augmented bandgap and the decreased surface defect density of the perov- skite layer also contribute to the significantly enhanced V_{oc} along with the better matching in device band level alignment. When x increases to 0.5, J_{sc} drops down to only 19.05 mA cm^{-2} while V_{oc} keeps similar although its bandgap is still enlarged. That variation can be attributed to the obvious augment of bandgap after a balance point in that trade off. Further increasing x to 1, all the three parameters decline sharply, which may subject to its poor intrinsic photovoltaic performance,[47,48] as well as the pinholes existed in our films. However, the con- version efficiency of 3.96% in our work demonstrates its device performance still benefit from the highly crystalline and orien- tation film. Moreover, the $MA_{0.25}FA_{0.75}SnI_{2.75}Br_{0.25}$ based device also shows the eliminated hysteresis in contrast to that control $FASnI_3$ one, as shown in Figure 3d, which may be ascribed to the restrained ions moving and accumulation across the device by the enhanced film quality and the improved energy level alignment at interfaces. Figure 3e shows the two typical devices' external quantum efficiency (EQE) spectra and their integrated J_{sc} values. Those of the control $FASnI_3$ and the $MA_{0.25}FA_{0.75}SnI_{2.75}Br_{0.25}$ based are 21.88 and 21.23 mA cm^{-2}, respectively, which are lower than the corresponding values obtained in J–V curves (Figure 3d). The slight underestimated J_{sc} may be due to the spectral mismatch between the two solar simulators involved. However, the difference in the drop tails of the two spectra clearly claims the augment of bandgap via the incorporation of MABr, which is consistent to the absorption spectra shown in Figure 2f. The photon–electron conversion efficiency across the whole absorption spectrum also examines the enhanced crystallinity and herein decreased trap density of the films. In addition, the optimal device based on $MA_{0.25}FA_{0.75}SnI_{2.75}Br_{0.25}$ film achieved a stabilized steady-state photocurrent of 19.45 mA cm^{-2} and output efficiency of 8.95% at a fixed bias of 0.46 V near the maximum power point, as displayed in Figure 3f. That proves the validity of our devices. Table S2, Supporting Information summarizes the detailed device perfor- mance parameters of the series of $MA_xFA_{1-x}SnI_{3-x}Br_x$ (x = 0, 0.15, 0.25, 0.5, and 1) perovskites.

As we know, the deep defects in p type mainly results from the oxidation of Sn^{2+} in a form of Sn vacancy.[17,25,26,49–51] To figure out the mechanism of the decreased defect density, which leads to the improved device performance, X-ray photoelectron spectroscopy (XPS) measurements of the pristine $FASnI_3$ and $MA_{0.25}FA_{0.75}SnI_{2.75}Br_{0.25}$ perovskite films were performed. The Sn 3d core XPS spectrum of the pristine $FASnI_3$ perovskite film in **Figure 4**a shows that the two peaks deconvoluted from the Sn $3d_{5/2}$ peak at 486.7 and 487.6 eV are attributed to Sn^{2+} and Sn^{4+}, respectively. While the corresponding Sn 3d peaks of the $MA_{0.25}FA_{0.75}SnI_{2.75}Br_{0.25}$ perovskite film obviously shift of ≈1 eV to lower binding energy, which can be attributed to the substitution of I^- by Br^-.[25] Strikingly, a significant decrease of the Sn^{4+} content from 14.3% to 8.6% is realized by the incorpo- ration of MABr (Table S3, Supporting Information). It quantita- tively defines the suppression effect of Sn^{2+} oxidation by MABr. The comparison of Br 3d core spectra of both films further veri- fies the presence of MABr in the $MA_{0.25}FA_{0.75}SnI_{2.75}Br_{0.25}$ films (Figure 4b and Figure S6, Supporting Information). The Br core level XPS spectra of the alloyed perovskite films with various MABr content (x = 0.25, 0.5, 1, respectively) are obtained by XPS measurement, showing in Figure S6, Supporting Infor- mation. With increased MABr content, gradually enhanced intensity of Br 3d peak can be obvious observed. The relative bad signal-to-noise ratio of $MA_{0.25}FA_{0.75}SnI_{2.75}Br_{0.25}$ film mainly caused by the low content of MABr. Furthermore, the F 1s XPS peak of $MA_{0.25}FA_{0.75}SnI_{2.75}Br_{0.25}$ perovskite film in Figure 4c apparently falls off in contrast to the spectra of pristine $FASnI_3$ film, indicating the elimination of the redundant SnF_2 flakes, and is also consistent with the surface morphology change in the SEM images (Figure 2).

The photoluminescence (PL) spectra of those films are shown in Figure 4d. The emission peak of $MA_{0.25}FA_{0.75}SnI_{2.75}Br_{0.25}$ perovskite film has a significant blue-shift to ≈860 nm in con- trast to that of the pristine $FASnI_3$ film (≈924 nm), consistent with the above absorption data and some previous reports.[25] In addition, the PL peak intensity of the $MA_{0.25}FA_{0.75}SnI_{2.75}Br_{0.25}$

perovskite film is apparently increased after MABr incorpo- ration, indicating the suppressed non-radiative trap-assisted recombination (Figure 4d).[52–54] Furthermore, the time-resolved PL spectra were measured and shown in Figure S7, Supporting Information, with the humidity of about 50% at ≈25 °C. The mixed $MA_{0.25}FA_{0.75}SnI_{2.75}Br_{0.25}$ film displayed beyond 2-fold longer time (3.52 ns) than that of the pristine $FASnI_3$ film (1.65 ns), further confirming the decreased trap state density after MABr incorporation.

To further evaluate the elimination effect of the trap states in the perovskite films by incorporating MABr, the space-charge limited current measurements were employed to identify the trap density in the perovskite films.[32,55] The hole-only devices were fabricated with a structure of ITO/Au/PEDOT:PSS/ $FASnI_3$/2,2′,7,7′-tetrakis[N,N-di(4-methoxyphenyl)amino]-9,9′-spirobifluorene (Spiro-OMeTAD)/Au. **Figure 5**a shows the *I*–*V* curves in the dark of both $FASnI_3$ and $MA_{0.25}FA_{0.75}SnI_{2.75}Br_{0.25}$-based devices in a double logarithmic scale. They clearly con- sist of three regions: Ohmic region at low bias, Trap-filled limit (TFL) region at middle bias, and Child region at high bias. The trap-state density (n_{trap}) can be calculated by the fol- lowing relation: $n_{trap} = 2\varepsilon\varepsilon_0 V_{TFL} eL^{-2}$, where ε_0 is the vacuum permittivity, ε is the relative dielectric constant (typically 35 for perovskites), V_{TFL} is the onset voltage of TFL region, e is the elementary charge, and L is the thickness of the perovskite film (≈0.3 ⌈m in these films). The V_{TFL} values of the $FASnI_3$ and $MA_{0.25}FA_{0.75}SnI_{2.75}Br_{0.25}$-based devices are around 0.27 and 0.14 V, respectively. The corresponding n_{trap} of the $FASnI_3$ and the $MA_{0.25}FA_{0.75}SnI_{2.75}Br_{0.25}$ films are estimated to be $6.98 \cdot 10^{15}$ and $3.58 \cdot 10^{15}$ cm^{-3}, respectively. It is obvious that the introduction of MABr results in a significant decline of the trap density. That coincides with the characterizations and device performances discussed above.

Figure 5b shows the light intensity dependent V_{oc} of the two devices based on $FASnI_3$ and $MA_{0.25}FA_{0.75}SnI_{2.75}Br_{0.25}$ perovskites. The $FASnI_3$ device exhibits a slope of 1.68kT/q, while that of the $MA_{0.25}FA_{0.75}SnI_{2.75}Br_{0.25}$ is 1.18 kT/q. As we know, the slope deviated from (kT/q) is closely related to trap-assisted recombination. The smaller slope of the $MA_{0.25}FA_{0.75}SnI_{2.75}Br_{0.25}$ device indicates smaller energy loss from trap-assisted recombination, compared with the control $FASnI_3$ one.[53,56] So, it confirms the perovskite trap density is significantly eliminated by the alloying of MABr, and finally results in the remarkably enhanced V_{oc} and FF in the based device performance.

Figure 6 shows the conversion efficiency distribution of the pristine $FASnI_3$ and $MA_{0.25}FA_{0.75}SnI_{2.75}Br_{0.25}$ PSCs in batch of 36 devices. The pristine $FASnI_3$ devices have an efficiency range from 2.91% to 5.02% with an average value of 3.98%. While $MA_{0.25}FA_{0.75}SnI_{2.75}Br_{0.25}$ PSCs have an impressed efficiency varies from 7.82% to 9.31% with an average value of 8.68% after 0.25 MABr incorporation. Moreover, the narrowing distribution indicates the improved process reproducibility with the MABr incorporation. Furthermore, the device stability is evaluated by continuous light soaking with simulated solar illumination (AM 1.5G, 100 mW cm^{-2}) and shown in Figure 6b, resulting in a utilization temperature of ca. 50 °C. The pristine $FASnI_3$ device shows a sharp degradation and failed after a duration of 120 h. Remarkably, the $MA_{0.25}FA_{0.75}SnI_{2.75}Br_{0.25}$ device still maintains above 80% of the initial efficiency after 300 h of light soaking, evidently indicating that the MABr incorporation effec- tively improves the light and thermal stability of the perovskite films and herein the whole device stability.

3. Conclusion

In summary, depending on the systematical composition engi- neering, we successfully obtained the optimized $FASnI_3$ perov-skites by the incorporation of MABr, $MA_{0.25}FA_{0.75}SnI_{2.75}Br_{0.25}$. In the alloying of MABr, MA^+ ions are responsible for the impressively orientated crystallization of the perovskite films while Br^- ions account for their bandgap modulation. Basing on high quality of $MA_{0.25}FA_{0.75}SnI_{2.75}Br_{0.25}$ perovskite films, the conversion efficiency surges to 9.31% in contrast to 5.02% of the control $FASnI_3$ device, along with big enhancements in V_{oc} and FF. Moreover, the device hysteresis is almost eliminated remarkably. XPS data reveal that the oxidation from Sn^{2+} to Sn^{4+} is strongly suppressed and herein leads to obvious reduc-tion of trap density by the incorporation of MABr, evidenced as well by the device physics measurements. That also results in the outstanding device stability, maintaining above 80% of the initial efficiency after 300 h of light soaking for the $MA_{0.25}FA_{0.75}SnI_{2.75}Br_{0.25}$ perovskite based devices while the control $FASnI_3$ device dies within 120 h. This work definitely demonstrates a facile and effective strategy to develop tin halide perovskites solar cells, optoelectronic devices and beyond.

Supporting Information

Supporting Information is available from the Wiley Online Library or from the author.

Acknowledgements

B.-B.Y. and M.L. contributed equally to this work. This work is supported by the National Natural Science Foundation of China (NSFC) (No. 61775091), Natural Science Foundation of Shenzhen Innovation Committee (No. JCYJ20180504165851864), and the Shenzhen Key Laboratory Project (No. ZDSYS201602261933302) and the authors thank the Core Research Facilities of SUSTech for some characterizations in this work.

Conflict of Interest

The authors declare no conflict of interest.

Adv. Funct. Mater. **2020**, *30*, 2002230

Keywords

divalent tin ions, methylammonium bromide, oriented crystallization, tin halide perovskites, trap density

References

[1] Best Research-Cell Efficiency Chart, https://www.nrel.gov/pv/cell- efficiency.html (accessed: January 2020).

[2] M. Liu, M. B. Johnston, H. J. Snaith, *Nature* **2013**, *501*, 395.
[3] N. J. Jeon, J. H. Noh, W. S. Yang, Y. C. Kim, S. Ryu, J. Seo, S. I. Seok, *Nature* **2015**, *517*, 476.
[4] Q. Jiang, L. Zhang, H. Wang, X. Yang, J. Meng, H. Liu, Z. Yin, J. Wu, X. Zhang, J. You, *Nat. Energy* **2017**, *2*, 16177.
[5] M. He, X. Pang, X. Liu, B. Jiang, Y. He, H. Snaith, Z. Lin, *Angew. Chem., Int. Ed.* **2016**, *55*, 4280.
[6] M. He, B. Li, X. Cui, B. Jiang, Y. He, Y. Chen, D. O'Neil, P. Szymanski, M. A. EI-Sayed, J. Huang, Z. Lin, *Nat. Commun.* **2017**, *8*, 16045.
[7] X. Meng, X. Cui, M. Rager, S. Zhang, Z. Wang, J. Yu, Y. W. Harn, Z. Kang, B. K. Wagner, Y. Liu, C. Yu, J. Qiu, Z. Lin, *Nano Energy* **2018**, *52*, 123.
[8] B. Wang, J. Iocozzia, M. Zhang, M. Ye, S. Yan, H. Jin, S. Wang, Z. Zou, Z. Lin, *Chem. Soc. Rev.* **2019**, *48*, 4854.
[9] J. Tong, Z. Song, D. H. Kim, X. Chen, C. Chen, A. F. Palmstrom, P. F. Ndione, M. O. Reese, S. P. Dunfield, O. G. Reid, J. Liu, F. Zhang, S. P. Harvey, Z. Li, S. T. Christensen, G. Teeter, D. Zhao, M. M. Al-Jassim, M. F. A. M. van Hest, M. C. Beard, S. E. Shaheen, J. J. Berry, Y. Yan, K. Zhu, *Science* **2019**, *364*, 475.

[10] N. K. Noel, S. D. Stranks, A. Abate, C. Wehrenfennig, S. Guarnera, A.-A. Haghighirad, A. Sadhanala, G. E. Eperon, S. K. Pathak, M. B. Johnston, A. Petrozza, L. M. Herz, H. J. Snaith, *Energy Environ. Sci.* **2014**, *7*, 3061.

[11] F. Hao, C. C. Stoumpos, D. H. Cao, R. P. H. Chang, M. G. Kanatzidis, *Nat. Photonics.* **2014**, *8*, 489.

[12] A. Abate, *Joule* **2017**, *1*, 659.
[13] S. B. Kang, J.-H. Kim, M. H. Jeong, A. Sanger, C. U. Kim, C.-M. Kim, K. J. Choi, *Light: Sci. Appl.* **2019**, *8*, 121.
[14] B.-B. Yu, M. Liao, J. Yang, W. Chen, Y. Zhu, X. Zhang, T. Duan, W. Yao, S.-H. Wei, Z. He, *J. Mater. Chem. A* **2019**, *7*, 8818.
[15] M. A. Kamarudin, D. Hirotani, Z. Wang, K. Hamada, K. Nishimura, Q. Shen, T. Toyoda, S. Iikubo, T. Minemoto, K. Yoshino, S. Hayase, *J. Phys. Chem. Lett.* **2019**, *10*, 5277.

[16] W. Liao, D. Zhao, Y. Yu, C. R. Grice, C. Wang, A. J. Cimaroli, P. Schulz, W. Meng, K. Zhu, R.-G. Xiong, Y. Yan, *Adv. Mater.* **2016**, *28*, 9333.

[17] T.-B. Song, T. Yokoyama, S. Aramaki, M. G. Kanatzidis, *ACS Energy Lett.* **2017**, *2*, 897.

[18] S. J. Lee, S. S. Shin, Y. C. Kim, D. Kim, T. K. Ahn, J. H. Noh, J. Seo, S. I. Seok, *J. Am. Chem. Soc.* **2016**, *138*, 3974.

[19] M. E. Kayesh, T. H. Chowdhury, K. Matsuishi, R. Kaneko, S. Kazaoui, J.-J. Lee, T. Noda, A. Islam, *ACS Energy Lett.* **2018**, *3*, 1584.

[20] H. Kim, Y. H. Lee, T. Lyu, J. H. Yoo, T. Park, J. H. Oh, *J. Mater. Chem. A* **2018**, *6*, 18173.

[21] T.-B. Song, T. Yokoyama, C. C. Stoumpos, J. Logsdon, D. H. Cao, M. R. Wasielewski, S. Aramaki, M. G. Kanatzidis, *J. Am. Chem. Soc.* **2017**, *139*, 836.

[22] Y. Dang, Y. Zhou, X. Liu, D. Ju, S. Xia, H. Xia, X. Tao, *Angew. Chem., Int. Ed.* **2016**, *55*, 3447.

[23] J. H. Heo, J. Kim, H. Kim, S. H. Moon, S. H. Im, K.-H. Hong, *J. Phys. Chem. Lett.* **2018**, *9*, 6024.

[24] X. Liu, K. Yan, D. Tan, X. Liang, H. Zhang, W. Huang, *ACS Energy Lett.* **2018**, *3*, 2701.

[25] S. J. Lee, S. S. Shin, J. Im, T. K. Ahn, J. H. Noh, N. J. Jeon, S. I. Seok, J. Seo, *ACS Energy Lett.* **2018**, *3*, 46.

[26] T. Shi, H.-S. Zhang, W. Meng, Q. Teng, M. Liu, X. Yang, Y. Yan, H.-L. Yip, Y.-J. Zhao, *J. Mater. Chem. A* **2017**, *5*, 15124.

[27] Z. Zhao, F. Gu, Y. Li, W. Sun, S. Ye, H. Rao, Z. Liu, Z. Bian, C. Huang, *Adv. Sci.* **2017**, *4*, 1700204.

[28] S. Shao, J. Liu, G. Portale, H.-H. Fang, G. R. Blake, G. H. ten Brink, L. J. A. Koster, M. A. Loi, *Adv. Energy Mater.* **2018**, *8*, 1702019.

[29] F. Wang, X. Jiang, H. Chen, Y. Shang, H. Liu, J. Wei, W. Zhou, H. He, W. Liu, Z. Ning, *Joule* **2018**, *2*, 2732.

[30] X. Liu, Y. Wang, F. Xie, X. Yang, L. Han, *ACS Energy Lett.* **2018**, *3*, 1116.

[31] E. Jokar, C.-H. Chien, C.-M. Tsai, A. Fathi, E. W.-G. Diau, *Adv. Mater.* **2019**, *31*, 1804835.

[32] F. Gu, S. Ye, Z. Zhao, H. Rao, Z. Liu, Z. Bian, C. Huang, *Sol. RRL* **2018**, *2*, 1800136.

[33] M. Xiao, S. Gu, P. Zhu, M. Tang, W. Zhu, R. Lin, C. Chen, W. Xu, T. Yu, J. Zhu, *Adv. Opt. Mater.* **2018**, *6*, 1700615.

[34] N. Wang, Y. Zhou, M.-G. Ju, H. F. Garces, T. Ding, S. Pang, X. C. Zeng, N. P. Padture, X. W. Sun, *Adv. Energy Mater.* **2016**, *6*, 1601130.

[35] C. Ran, W. Gao, J. Li, J. Xi, L. Li, J. Dai, Y. Yang, X. Gao, H. Dong, B. Jiao, I. Spanopoulos, C. D. Malliakas, X. Hou, M. G. Kanatzidis, Z. Wu, *Joule* **2019**, *3*, 3072.

[36] M. Chen, M.-G. Ju, H. F. Garces, A. D. Carl, L. K. Ono, Z. Hawash, Y. Zhang, T. Shen, Y. Qi, R. L. Grimm, D. Pacifici, X. C. Zeng, Y. Zhou, N. P. Padture, *Nat. Commun.* **2019**, *10*, 16.

[37] K. P. Marshall, M. Walker, R. I. Walton, R. A. Hatton, *Nat. Energy* **2016**, *1*, 16178.

[38] M. H. Kumar, S. Dharani, W. L. Leong, P. P. Boix, R. R. Prabhakar, T. Baikie, C. Shi, H. Ding, R. Ramesh, M. Asta, M. Graetzel, S. G. Mhaisalkar, N. Mathews, *Adv. Mater.* **2014**, *26*, 7122.

[39] T. Wu, X. Liu, X. He, Y. Wang, X. Meng, T. Noda, X. Yang, L. Han, *Sci. China: Chem.* **2020**, *63*, 107.

[40] P. Li, X. Liu, Y. Zhang, C. Liang, G. Chen, F. Li, M. Su, G. Xing, X. Tao, Y. Song, *Angew. Chem., Int. Ed.* **2020**, *59*, 6909.

[41] A. M. Boehm, T. Liu, S. M. Park, A. Abtahi, K. R. Graham, *ACS Appl. Mater. Interfaces* **2020**, *12*, 5209.

[42] D. B. Khadka, Y. Shirai, M. Yanagida, K. Miyano, *J. Mater. Chem. C* **2020**, *8*, 2307.

[43] W.-F. Yang, F. Igbari, Y.-H. Lou, Z.-K. Wang, L.-S. Liao, *Adv. Energy Mater.* **2019**, *9*, 1902584.

[44] X. Zheng, C. Wu, S. K. Jha, Z. Li, K. Zhu, S. Priya, *ACS Energy Lett.* **2016**, *1*, 1014.

[45] Y. Reyna, M. Salado, S. Kazim, A. Pérez-Tomas, S. Ahmad, M. Lira-Cantu, *Nano Energy* **2016**, *30*, 570.

[46] G. Liu, H. Zheng, L. Zhu, A. Alsaedi, T. Hayat, X. Pan, L. e. Mo, S. Dai, *ChemSusChem* **2018**, *11*, 2436.

[47] C.-M. Tsai, N. Mohanta, C.-Y. Wang, Y.-P. Lin, Y.-W. Yang, C.-L. Wang, C.-H. Hung, E. W.-G. Diau, *Angew. Chem.* **2017**, *129*, 14007.

[48] T. Yokoyama, T.-B. Song, D. H. Cao, C. C. Stoumpos, S. Aramaki, M. G. Kanatzidis, *ACS Energy Lett.* **2017**, *2*, 22.

[49] I. Chung, J.-H. Song, J. Im, J. Androulakis, C. D. Malliakas, H. Li, A. J. Freeman, J. T. Kenney, M. G. Kanatzidis, *J. Am. Chem. Soc.* **2012**, *134*, 8579.

[50] P. Xu, S. Chen, H.-J. Xiang, X.-G. Gong, S.-H. Wei, *Chem. Mater.* **2014**, *26*, 6068.

[51] Z. Xiao, Z. Song, Y. Yan, *Adv. Mater.* **2019**, *31*, 1803792.
[52] B.-B. Yu, L. Xu, M. Liao, Y. Wu, F. Liu, Z. He, J. Ding, W. Chen, B. Tu, Y. Lin, Y. Zhu, X. Zhang, W. Yao, A. B. Djurišić, J.-S. Hu, Z. He, *Sol. RRL* **2019**, *3*, 1800290.
[53] W. Chen, Y. Zhou, G. Chen, Y. Wu, B. Tu, F.-Z. Liu, L. Huang, A. M. C. Ng, A. B. Djurišić, Z. He, *Adv. Energy Mater.* **2019**, *9*, 1803872.
[54] M. Liao, B.-B. Yu, Z. Jin, W. Chen, Y. Zhu, X. Zhang, W. Yao, T. Duan, I. Djerdj, Z. He, *ChemSusChem* **2019**, *12*, 5007.
[55] W. Chen, K. Li, Y. Wang, X. Feng, Z. Liao, Q. Su, X. Lin, Z. He, *J. Phys. Chem. Lett.* **2017**, *8*, 591.
[56] K. Chen, P. Wu, W. Yang, R. Su, D. Luo, X. Yang, Y. Tu, R. Zhu, Q. Gong, *Nano Energy* **2018**, *49*, 411.

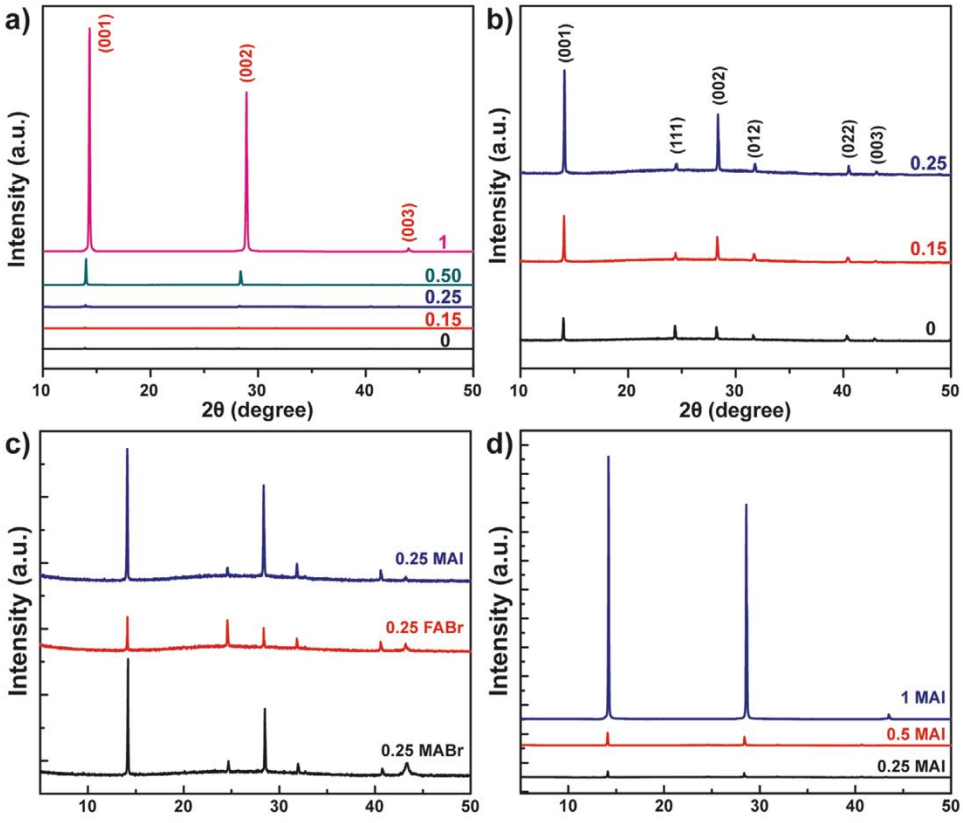

Figure 1. a) XRD patterns of $MA_xFA_{1-x}SnI_{3-x}Br_x$ perovskite films (x = 0, 0.15, 0.25, 0.5, 1) with different contents of MABr. b) Magnified XRD patterns of $MA_xFA_{1-x}SnI_{3-x}Br_x$ perovskites with low contents of MABr (x = 0, 0.15, 0.25). c) XRD patterns of perovskites with different components. d) XRD patterns of $MA_xFA_{1-x}SnI_3$ perovskite films with different contents of MAI (x = 0.25, 0.5, 1).

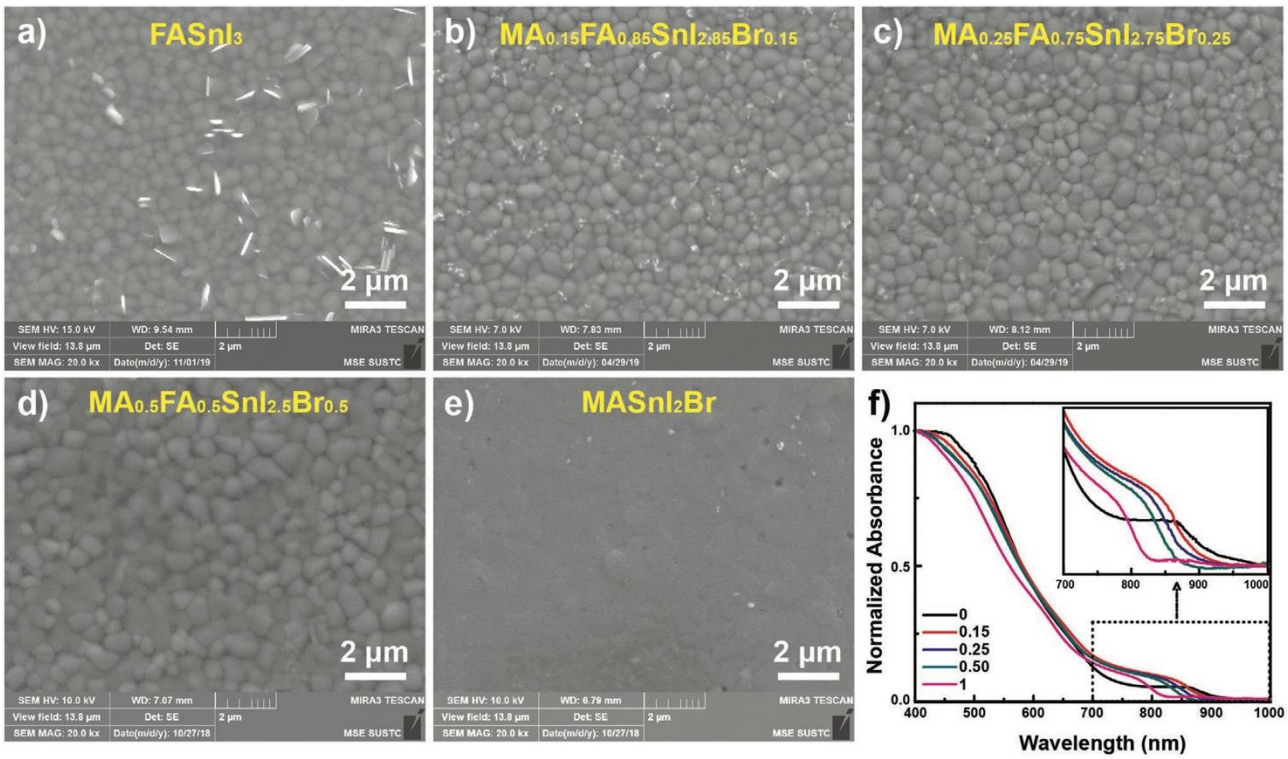

Figure 2. a–e) Top-view SEM images of $MA_xFA_{1-x}SnI_{3-x}Br_x$ perovskite films with x = 0, 0.15, 0.25, 0.50, 1.0. f) Normalized UV–vis absorbance spectra of corresponding films.

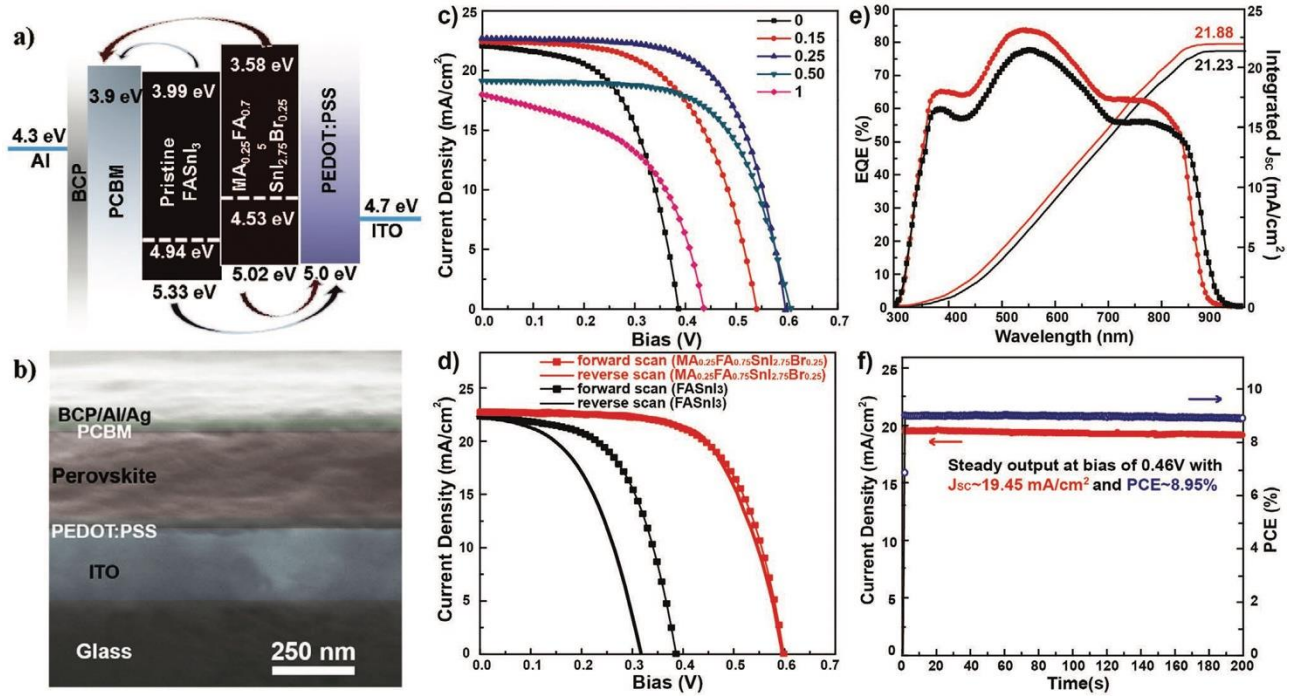

Figure 3. a) Energy band alignment of the inverted planar PSCs containing both $FASnI_3$ film and $MA_{0.25}FA_{0.75}SnI_{2.75}Br_{0.25}$ perovskite films. b) Cross- sectional SEM image of the typical $MA_{0.25}FA_{0.75}SnI_{2.75}Br_{0.25}$ device. c) The *J–V* curves of champion devices for $MA_xFA_{1-x}SnI_{3-x}Br_x$ perovskites with $x = 0$, 0.15, 0.25, 0.50, 1.0. d) The *J–V* curves of champion devices based of pristine $FASnI_3$ film and $MA_{0.25}FA_{0.75}SnI_{2.75}Br_{0.25}$ film for both forward and reverse scans. e) Typical EQE spectra of the pristine $FASnI_3$ and $MA_{0.25}FA_{0.75}SnI_{2.75}Br_{0.25}$ perovskite devices. f) Steady photocurrent output at fixed bias and steady PCE of the optimal device.

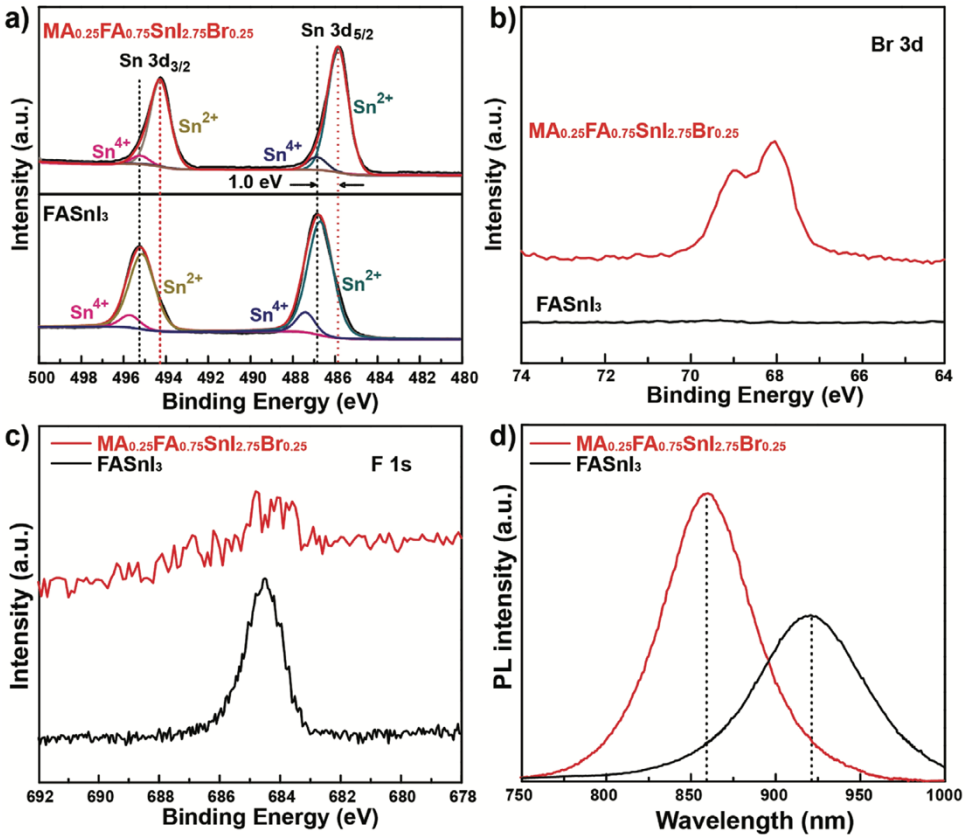

Figure 4. XPS spectra of a) Sn 3d, b) Br 3d, c) F 1s, and d) photoluminescence (PL) spectra of pristine $FASnI_3$ film and $MA_{0.25}FA_{0.75}SnI_{2.75}Br_{0.25}$ perovskite film.

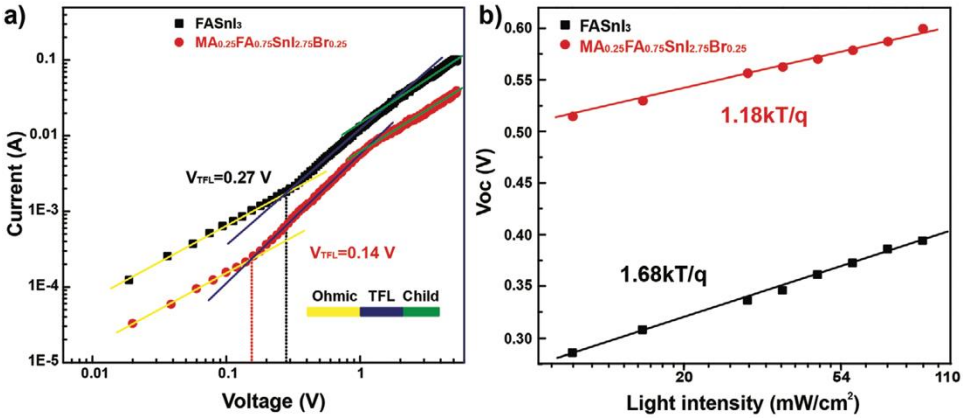

Figure 5. a) Hole-only devices for measurement of the trap-state density of the pristine $FASnI_3$ film and $MA_{0.25}FA_{0.75}SnI_{2.75}Br_{0.25}$ perovskite film. b) Linear relationship of V_{oc} with respect to the logarithmic light intensity for devices without and with MABr ($x = 0.25$).

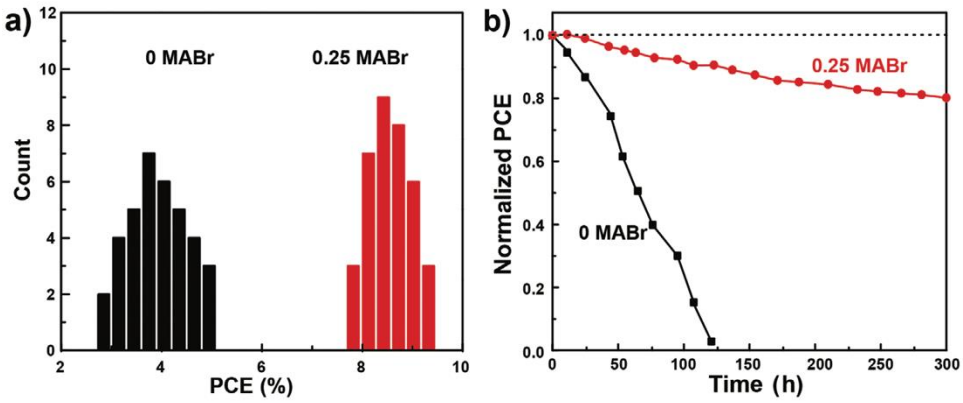

Figure 6. a) The conversion efficiency distribution of devices based on pristine $FASnI_3$ film and $MA_{0.25}FA_{0.75}SnI_{2.75}Br_{0.25}$ perovskite film. The sample size is 36 in both cases. b) Corresponding light soaking tests for both PSCs without and with MABr under a continuous simulated solar irradiation (AM 1.5G, 100 mW cm^{-2}).